Low-altitude Terrestrial Spectroscopy from a Pushbroom Sensor

Juan-Pablo Ramirez-Paredes
Department of Electrical Engineering, University of Texas at Dallas, 800 West Campbell Road, Richardson, Texas 75080
e-mail: pablo.ramirez@utdallas.edu
David Lary
Department of Physics, The University of Texas at Dallas, 800 West Campbell Road, Richardson, Texas 75080
e-mail: david.lary@utdallas.edu
Nicholas Gans
Department of Electrical Engineering, University of Texas at Dallas, 800 West Campbell Road, Richardson, Texas 75080

Hyperspectral cameras sample many different spectral bands at each pixel, enabling advanced detection and classification algorithms. However, their limited spatial resolution and the need to measure the camera motion to create hyperspectral images makes them unsuitable for nonsmooth moving platforms such as unmanned aerial vehicles (UAVs). We present a procedure to build hyperspectral images from line sensor data without camera motion information or extraneous sensors. Our approach relies on an accompanying conventional camera to exploit the homographies between images for mosaic construction. We provide experimental results from a low-altitude UAV, achieving high-resolution spectroscopy with our system. © 2015 Wiley Periodicals, Inc.

1. INTRODUCTION

While digital cameras are useful as airborne sensors for terrestrial surveying, the spectral information contained in their images is limited to a few broad bands, typically one for grayscale imaging or three-color imaging. Multispectral cameras partially overcome this limitation, but they are also restricted in the quantity and breadth of the frequency bands they make available per picture element. In contrast, hyperspectral cameras provide potentially hundreds of different spectral bands per pixel. Since the 1970s, when field measurements were made supporting the analysis of Landsat-1 observations, imaging spectroscopy via hyperspectral cameras has steadily progressed (Goetz, 2009).

There have been many applications of hyperspectral sensors in imaging of land, ocean, and atmospheric composition. In precision farming, it is possible to model the response of plants to factors such as drought, disease, or pollution by analyzing the reflectance and absorption of specific spectral wavelengths (Smith, Steven, & Colls, 2004). There have also been successful studies of mineral identification by processing hyperspectral data from instruments such as the Airborne Visible/Infrared Imaging Spectrometer (AVIRIS) (Kruse, Boardman, & Huntington, 2003). Oil spills such as the Deepwater Horizon incident of 2010 can also be precisely delimited by spectroscopy (Sidike, Khan, Alam, & Bhuiyan, 2012). There have been attempts at characterizing human skin from hyperspectral data to get an accurate identification of pedestrians, setting a precedent for surveillance or search-and-rescue applications (Herweg, Kerekes, & Eismann, 2012).

To enable imaging at hundreds of distinct frequency bands, the optics of hyperspectral sensors are significantly different from a typical digital camera. Hyperspectral cameras are typically line-scanning and record the spectrum at all channels corresponding to a single image line in space. An example of a hyperspectral image is seen in Figure 1. Given the narrow collimation slit of the optics, a single hyperspectral image is often of limited use since it has a very small field of view in one direction. Hyperspectral sensor technology has progressed toward solutions that allow two-dimensional (2D) frame capture, where each pixel has an associated set of frequency responses. Recent developments, such as the Fabry-Pérot interferometer camera, have the potential to replace line-scanning cameras (Honkavaara et al., 2013). However, the line-scan variety is reliable, commercially available, has no moving parts, and remains the lowest in cost and complexity (Vagni, 2007). Line-scan hyperspectral cameras typically have finer spectral resolution than their full-frame counterparts, and generally cover a wider spectrum in each capture. Therefore, line-scan cameras still address the widest range of useful data analysis and applications.

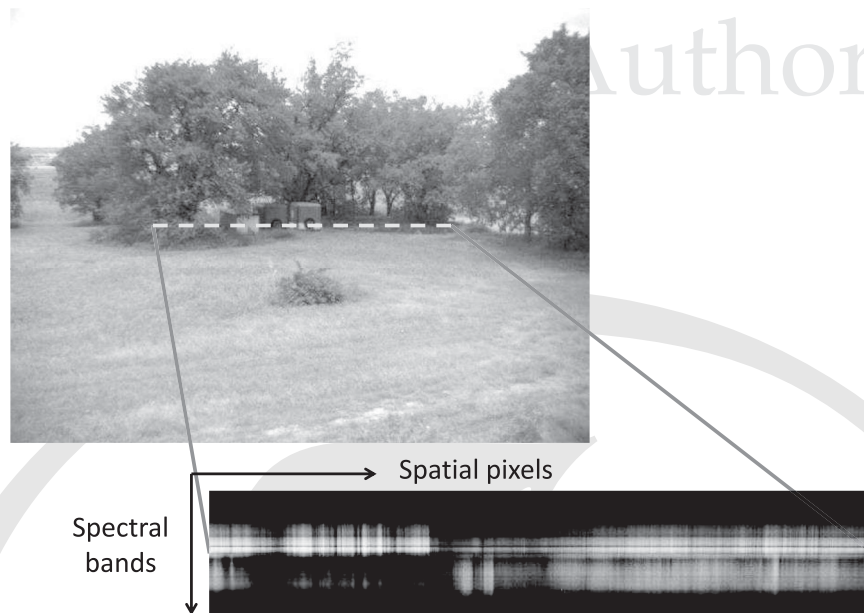Direct correspondence to: Nicholas Gans, e-mail: ngans@utdallas.edu

Figure 1. Comparison of a hyperspectral image line with a section of a visible light, conventional camera image. The cameras are positioned side by side, and the dashed line corresponds to the line captured by the hyperspectral camera.

If the hyperspectral camera is moved at a precise speed orthogonal to the scan line and consistent with the camera frame rate, the scan lines can be compiled and processed into a single image. Ideally, the imaging line moves one pixel per sample time in a direction perpendicular to the line, and the collected data are a proper image. Therefore, this is often referred to as "pushbroom imaging" and "pushbroom camera."[1] Typically, interpolation is performed to compensate for imprecise motion. This approach generally requires high altitude aircraft or Earth-orbiting instruments. Relevant examples with aircraft include that in Asmat, Milton, & Atkinson (2011), which imaged 32 spectral bands over farmland from an aircraft flying steadily at 1,900 m, and that in Schechner & Nayar (2002), which involved a camera imaging 21 spectral bands, moving precisely in a controlled lab environment. An example of a pushbroom hyperspectral camera not mounted on aircraft is presented in Monteiro, Minekawa, Kosugi, Akazawa, & Oda (2007), in which a crane was used as a platform to mount the sensor. In all cases, the pushbroom camera must be moved smoothly and at a constant speed.

There are many advantages to using unmanned aerial vehicles (UAVs) in place of or in conjunction with satellites. Due to their low flight altitude, better resolution can be achieved from the instruments they carry in terms of the number of "pixels on target." Data capture for a given area can be scheduled on demand, and the cost of the whole platform is considerably lower when compared with larger aircraft or Earth-orbiting equipment. The payload is also easily changed or upgraded according to application demands. However, using a line-scan sensor to perform pushbroom imaging on a non-smoothly-moving platform such as a UAV is a nontrivial task, given the difficulty of recovering the exact motion of the camera over time. There are different classes of UAVs, the main two being helicopters and airplanes. The helicopter class, including multirotor UAVs, is the most challenging for pushbroom imaging due to the fact that they have to tilt in order to move. They are also subject to vibration from their motors. Airplane UAVs can achieve steadier flight, but those with smaller wingspans are more prone to suffer from disturbances such as wind.

The precision and accuracy of localization sensors needs to be higher for a small UAV, since it is subjected to abrupt motions from internal and external sources, with an associated increase in cost. Spectroscopy has been achieved on these platforms by fusing inertial measurements and data from the global positioning system (Hruska, Mitchell, Anderson, & Glenn, 2012; Lucieer, Malenovský, Veness, & Wallace, 2014; Zarco-Tejada, González-Dugo, & Berni, 2012). In each of these works, the main problem is the level of accuracy of the inertial sensors of the UAVs. A workaround for this limitation is to complement the onboard sensor data with ground control points captured by a camera and to apply computer vision techniques to match pixels across images (Turner, Lucieer, & Watson, 2012). This is a

---

[1]While we present a method to generate hyperspectral images while not sweeping in a straight line, we will maintain the common convention of calling such cameras "pushbroom" cameras.

successful way to georeference data from frame imagers, but it does not apply to line-scanning sensors.

We propose a novel approach to enable a pushbroom hyperspectral camera to be used from a UAV, despite the aforementioned challenges. Furthermore, we do not require the addition of inertial sensors or external measurements of the camera pose. This is accomplished by using a conventional digital camera[2] rigidly attached close to the hyperspectral camera to provide additional information with which to build the hyperspectral image.

We focus on computer vision techniques, providing a direct map between the hyperspectral scanlines and the conventional camera images. With conventional cameras, it is possible to stitch together different views of a scene by means of the image homography. This process is typically called *image mosaicing* (Caballero, Merino, Ferruz, & Ollero, 2009; Szeliski, 1996). Computation of the homography requires point correspondences from two views of a planar object or scene and relates point projections in both camera views. The homography contains information about the rotation and translation of one camera view relative to the other, and by exploiting this our approach builds a hyperspectral image from a collection of hyperspectral lines mapped to a mosaic created from conventional camera images. Recent work focused on correlation-based alignment of pushbroom camera images (Moroni, Dacquino, & Cenedese, 2012). The ability of such a technique to cope with perspective transformations is limited, so its performance would be compromised in the presence of pitch or roll motions from the aircraft. As we show in the results, our approach can deal with a wide set of camera motions.

The work presented herein is an extension of that of Ramirez-Paredes, Lary, & Gans (2013), in which the concepts of this paper were introduced, accompanied by experimental results retrieved by hand-held operation of the sensor array. This paper presents new results from the use of a low-altitude UAV in conjunction with the sensor array to capture long image sequences exceeding 200 frames.

The rest of this paper is organized as follows: Section 2 explains how the intrinsic parameters of the hyperspectral camera are computed. Section 3 deals with the necessary aspects of designing a rig to mount the hyperspectral and conventional cameras, detailing restrictions on positioning the cameras and the method for aligning them. Section 4 explains how to map the pixels captured by the hyperspectral camera to their corresponding line in the conventional camera frame. Section 5 describes the construction of an image mosaic for the conventional camera and leveraging that mosaic, along with the results of the previous

---

[2]By "conventional digital camera" we mean a two-dimensional sensor with a rectangular grid as its image plane, where each element is sensitive to light in a broad band of frequencies hundreds of nanometers wide.

sections, to obtain a hyperspectral image. Experimental results are shown in Section 6, followed by a discussion in Section 7.

2. HYPERSPECTRAL CAMERA GEOMETRIC CALIBRATION

The typical approach to geometrically calibrate line sensors, such as hyperspectral cameras, is to attach them to a mechanical platform able to perform precise movements in a direction perpendicular to the scan line (Draréni, Roy, & Sturm, 2011; Gupta & Hartley, 1997). If the line sensor moves at a constant speed while imaging a known calibration target, stacking the image lines results in a full image. With this approach, the calibration procedure is similar to conventional camera techniques.

Our approach to geometrical calibration is mathematically similar to that in Gupta & Hartley (1997). However, their calibration method requires a moving camera (or a moving known target) with accurate measurements of velocity. Our method does not require any such motions, so it simplifies *ex situ* calibration. We model the hyperspectral camera as a conventional camera with one row of pixels, and every pixel is capable of measuring the intensity of several spectral bands. This approximation simplifies the camera model, yet it provides precise results.

We perform geometric calibration by capturing images of a special target. This provides a correspondence between world points with known coordinates and their projections on the pushbroom camera scanline, allowing for the recovery of parameters such as the field of view and the principal point. This same target is also used to align the hyperspectral and conventional cameras in our array, as will be detailed in the next section.

Consider a Cartesian frame $\mathcal{F}_h$ attached to the hyperspectral camera, with the origin at the camera focal point, the X axis parallel to the spatial pixels direction, the Y axis perpendicular to the spatial pixels direction, and the Z axis aligned with the line going from the focal point to the image line center and normal to the image line. Another Cartesian frame $\mathcal{F}_t$ is associated with the target. The target has a special pattern on the surface, containing a number of high contrast features we call *control points* with known coordinates in $\mathcal{F}_t$. It is essential that all control points not be collinear in 3D Cartesian space. For such a configuration there is an ambiguity, and a certain image of the points can arise from an infinite number of camera poses. Therefore, we suggest a target consisting of control points on two intersecting perpendicular lines.

In this work, we designed a target consisting of a thin, rigid, planar plastic sheet approximately 3 mm thick with a triangular shape. There is an alternating pattern of black and white bars on two edges that provides easily detectable transitions in the hyperspectral image, which constitute the control points. The separation between these points is 30 mm.
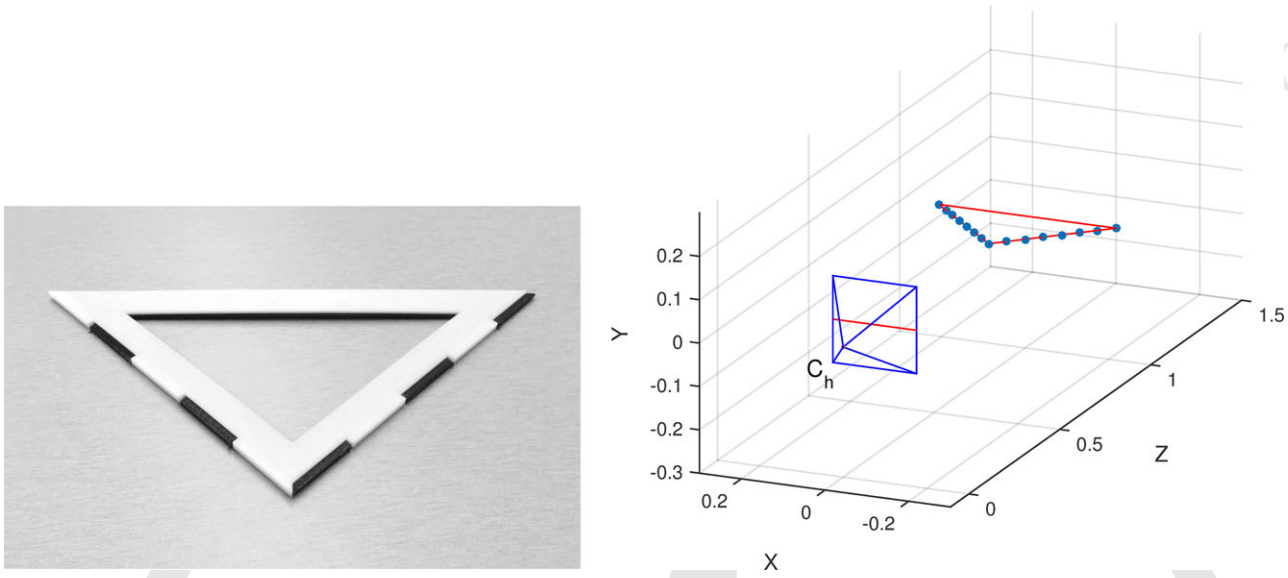
Figure 2. Left: the geometric calibration target used for the hyperspectral camera. Right: the calibration target along with the hyperspectral camera. The pyramid (C_h) represents the hyperspectral camera as in the pinhole model, with its scan line in red.

The target consists of two pieces of acrylonitrile-butadiede-styrene (ABS) plastic built from a 3D printer with a resolution of 0.254 mm. The target frame $\mathcal{F}_t$ has its X and Z axes as the intersecting lines containing the control points. We assume that the collimation slit of the hyperspectral camera is aligned with the pixel rows of its imaging sensor. If the target is currently aligned with the slit, the dark and white bands can detected in the hyperspectral image and the control points extracted.

The calibration target is shown in Figure 2, along with a diagram of the hyperspectral camera and the control points on a target. Any rotation of the target along the X or Y axes with respect to $\mathcal{F}_h$ will result in one or more control points not being projected into the scan line. Figure 3 simulates the difference between a correctly aligned target and a rotated one. A rotation of 1 degree on both the X and Y axes of $\mathcal{F}_h$ is shown. When the hyperspectral camera and the target are properly aligned, the projected control points (crosses) lie on the camera line, and they can all be detected. The rotations cause the projected points (squares) to fall outside of this line, making them not detectable.

Let us assume that no points are outside of the XZ plane of $\mathcal{F}_h$, since they could not be imaged otherwise. For simplicity, and without loss of generality, assume the target frame $\mathcal{F}_t$ is the world/inertial frame $\mathcal{F}_w$. The homogeneous coordinates of a point in $\mathcal{F}_w$ are $\mathbf{M} = [X\ 0\ Z\ 1]^T$, and the homogeneous transformation from the world frame to the $\mathcal{F}_h$ camera frame is denoted by $T_w^h \in SE(3)$ (i.e., the space of rigid body motions). A projection model from the world to the hyperspectral camera is given by

$$\lambda \mathbf{u} = K \Pi_0 T_w^h \mathbf{M}. \tag{1}$$

The projection of the point is $\lambda \mathbf{u} = \lambda [u\ 1]^T$, with λ being an unknown scale factor. K is a calibration matrix given by

$$K = \begin{bmatrix} f & u_0 \\ 0 & 1 \end{bmatrix}$$

with f being the horizontal focal length of the camera and u_0 its principal point in the horizontal direction. The matrix Π_0 is a projection given by

$$\Pi_0 = \begin{bmatrix} 1 & 0 & 0 & 0 \\ 0 & 0 & 1 & 0 \end{bmatrix}.$$

Following the developments for conventional cameras, it is possible to adapt the direct linear transform (DLT) (Abdel-Aziz, 1971) approach to the pushbroom camera. Just as the original DLT inverts a map $P_2 : \mathbb{P}^3 \to \mathbb{P}^2$, the pushbroom case requires an inversion of a map $P_1 : \mathbb{P}^2 \to \mathbb{P}$. Choosing the control points of the calibration target to be on the same plane as the hyperspectral camera line and focal point, it is possible to discard the Y coordinate of the points by setting it to zero.

As the frames $\mathcal{F}_w$ and $\mathcal{F}_h$ must have their Y-axes aligned, the rotation in T_w^h must have the form

$$T_w^h = \begin{bmatrix} \cos\theta & 0 & \sin\theta & t_x \\ 0 & 1 & 0 & 0 \\ -\sin\theta & 0 & \cos\theta & t_z \\ 0 & 0 & 0 & 1 \end{bmatrix},$$

where θ is the angle between the X axes of $\mathcal{F}_h$ and $\mathcal{F}_w$.

Considering that $Y = 0$ for every point, let us multiply $\Pi_0 T_w^h$ and discard the Y dimension in our computations, as it does not contribute to the projection. This gives rise to the
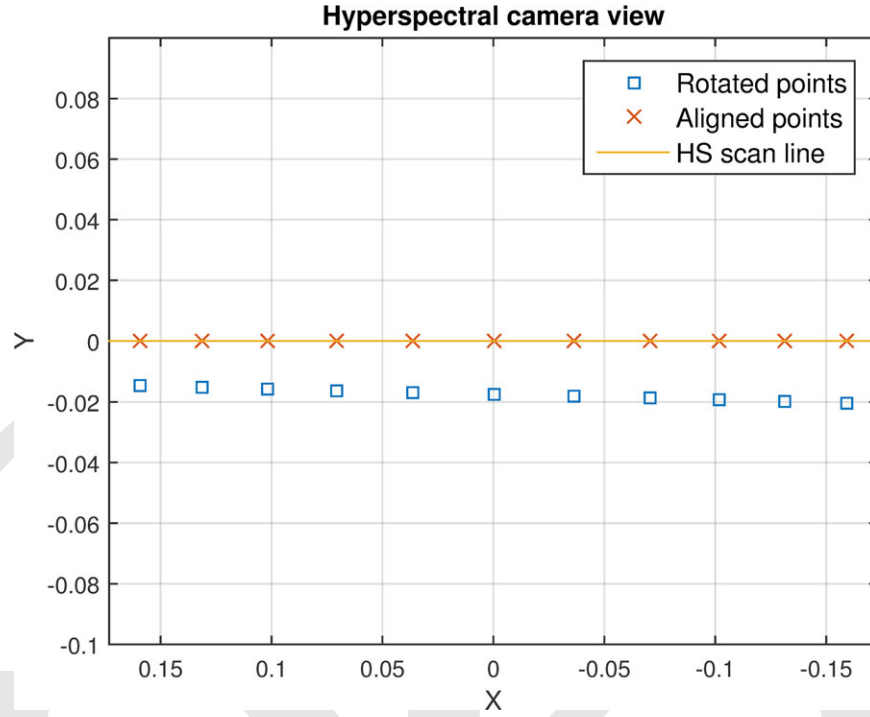
Hyperspectral camera view

Figure 3. Calibration target points projected on the hyperspectral camera. Only when the control points lie over the scan line are they visible to the camera.

simplified projection equation

$$\lambda \mathbf{u} = \begin{bmatrix} f & u_0 \\ 0 & 1 \end{bmatrix} \begin{bmatrix} \cos\theta & \sin\theta & t_x \\ -\sin\theta & \cos\theta & t_z \end{bmatrix} \begin{bmatrix} X \\ Z \\ 1 \end{bmatrix} = K \begin{bmatrix} R & \mathbf{t} \end{bmatrix} \mathbf{X},$$

(2)

where $R \in \mathcal{SO}(2)$ and $\mathbf{t} \in \mathbb{R}^2$. The intrinsic parameters of the camera are f and u_0 and determine the relationship between pixel and image plane coordinates. The extrinsic parameters define the pose of the camera with respect to the known world frame, $\mathcal{F}_w$. The intrinsic and extrinsic parameters can be combined to give a camera matrix that has six unknowns as

$$\lambda \mathbf{u} = \begin{bmatrix} a_1 & a_2 & a_3 \\ a_4 & a_5 & a_6 \end{bmatrix} \begin{bmatrix} X \\ Z \\ 1 \end{bmatrix} = A\mathbf{X}.$$

(3)

To cancel the scaling factor λ and rewrite the equations as a homogeneous linear system, we multiply both sides of Eq. (3) by $\mathbf{u}^T Q$, where Q is a skew-symmetric matrix given by

$$Q = \begin{bmatrix} 0 & -1 \\ 1 & 0 \end{bmatrix},$$

thus getting

$$\mathbf{u}^T Q A\mathbf{X} = 0.$$

(4)

Arranging the terms, the resulting equation gives

$$X a_1 + Z a_2 + a_3 - uX a_4 - uZ a_5 - u a_6 = 0.$$

Stacking equations for five or more point matches between the control points in $\mathcal{F}_t$ and their projection on the hyperspectral camera line gives the homogeneous system

$$\begin{bmatrix} X_1 & Z_1 & 1 & -u_1 X_1 & -u_1 Z_1 & -u_1 \\ X_2 & Z_2 & 1 & -u_2 X_2 & -u_2 Z_2 & -u_2 \\ \vdots & \vdots & \vdots & \vdots & \vdots & \vdots \\ X_n & Z_n & 1 & -u_n X_n & -u_n Z_n & -u_n \end{bmatrix} \begin{bmatrix} a_1 \\ a_2 \\ \vdots \\ a_6 \end{bmatrix} = 0.$$

(5)

$$S A_s = 0.$$

(6)

The matrix S can be at most of rank 5, so A_s can be solved up to a scale factor by finding the nullspace of the matrix S. From Eq. (2), we see that $a_4^2 + a_5^2 = 1$, so the proper scale α can be recovered up to a sign ambiguity as

$$\alpha = \pm \frac{1}{\sqrt{a_4^2 + a_5^2}}.$$

Once the matrix S has been properly scaled, the intrinsic and extrinsic parameters can be recovered as

$$u_0 = a_1 a_4 + a_2 a_5,$$

$$f = \left[a_1^2 + a_2^2 - u_0^2 \right]^{1/2}.$$

Either choice of sign for α results in the same parameters f and u_0. However, the different sign choice leads to two solutions for R and $\mathbf{t}$. Picking either α, the recovered poses are

$$R_1 = \begin{bmatrix} a_5 & -a_4 \\ a_4 & a_5 \end{bmatrix},$$

$$R_2 = R_1^T,$$

$$\mathbf{t}_1 = \begin{bmatrix} (a_3 - u_0 a_6)/f \\ a_6 \end{bmatrix},$$

$$\mathbf{t}_2 = -\mathbf{t}_1.$$

One solution will have a negative value for t_z. Since this would correspond to the control points being behind the camera, we can discard this translation and consider the positive t_z. Likewise, one rotation would be equivalent to the camera facing a direction opposite to the target.

We also address the issues of radial distortion and image noise. Radial distortion is a lens-induced phenomenon that causes deviation from rectilinear projection. It is typically modeled as a polynomial of even degree, where the only nonzero coefficients are those of even powers (Brown, 1966; Salvi, Armangué, & Batlle, 2002). For the case of the pushbroom camera, radial distortion can be modeled as

$$u_d = u + \kappa_1(u - u_0)^2 + \kappa_2(u - u_0)^4 + \mathcal{H.O.T.} \tag{7}$$

The distorted point projection is u_d, while the projection predicted by the pinhole model is given by u, and $\kappa_1, \kappa_2, \ldots$ are distortion coefficients. The number of coefficients to use depends on the degree of precision required. One coefficient provides acceptable results for our application. The distortion coefficient can be determined, and the camera parameters refined, by using convex nonlinear optimization, with the results obtained from the DLT part of the calibration as initialization values for the Levenberg-Marquardt algorithm (Zhang, 2000). Taking m images of the calibration target and locating the n control points in each, the measure to be minimized is the point reprojection error,

$$J_d(\mathbf{u}_p, \mathbf{u}'_p, \kappa_1) = \sum_{i=1}^{n} \sum_{j=1}^{m} ||u_i^j - u_i^{j'}||^2. \tag{8}$$

The vector $\mathbf{u}_p \in \mathbb{R}^{nm}$ contains the projections of the calibration points as predicted by our model using the hyperspectral camera parameters, while $\mathbf{u}'_p \in \mathbb{R}^{nm}$ are the actual projections of the calibration points. The point u_i^j represents the ith point of the jth calibration target image.

Another important procedure related to the hyperspectral camera is the precise determination of its spectral sensitivities. This procedure is known as radiometric calibration. This type of calibration generally requires measurements of special light sources for different integration times by the hyperspectral camera, under precise laboratory conditions (Zarco-Tejada et al., 2012). A related approach is to use a field spectroradiometer, which is a calibrated instrument that measures the reflectance of a particular object under field conditions (Al-Moustafa, Armitage, & Danson, 2012; Stratoulias, Balzter, Zlinszky, & Tóth, 2015). The light reflectance of the target objects is measured under outdoor lighting and then compared to the spectral response of the same targets as seen by the hyperspectral camera. This is done prior to the data collection flights. Our laboratory is not equipped to perform the radiometric calibration of the hyperspectral camera, so we relied on spectral sensitivity data from the camera manufacturer. This is sufficient to demonstrate and assess the hyperspectral imagery that our approach is able to create, but more precise calibration will need to be performed before application in dedicated studies of the environment.

3. CAMERA ARRAY ALIGNMENT

Our approach requires an accurate mapping between the pixels in the pushbroom line and the pixels in the conventional camera. Given the projection of a world point on one of the cameras, it is generally not possible to predict its projection on the other camera without knowing the depth of the point with respect to either of the cameras. However, under certain alignment conditions, epipolar geometry allows us to predict the line along which that point will be found (Hartley & Zisserman, 2003). This is a line-to-line map that generally depends on the depth of the world points in the camera frames. However, the correspondence can be uniquely determined if the hyperspectral line coincides with an epipolar line.

In projective geometry, using the pinhole camera model, elements of $\mathbb{R}^3$ can be used as homogeneous coordinates to represent both lines and points on the image plane. For points, the vector $\mathbf{p} = [u\ v\ 1]^T$ represents the coordinates of a point in the image plane; typically this denotes the intersection of the image plane and a ray of light from a 3D point through the focal point of the camera. The implicit equation for a line $au + bv + c = 0$ leads to a line representation $\mathbf{l} = [a\ b\ c]^T$. A given point $\mathbf{p}$ is part of a line $\mathbf{l}$ iff $\mathbf{p}^T \mathbf{l} = 0$. Thus, the hyperspectral camera line can be expressed as $\mathbf{l}_h = [0\ 1\ 0]^T$ in homogeneous coordinates in $\mathcal{F}_h$, since only points $\mathbf{p} = [u\ 0\ 1]^T$ belong to it. By our hyperspectral camera model in Eq. (1), only points with 3D homogeneous coordinates $\mathbf{X} = [X\ 0\ Z\ 1]^T$ in $\mathcal{F}_h$ frame can have a projection in the hyperspectral image. The projections of these points to the hyperspectral imaging surface lie on $\mathbf{l}_h$.

Consider the hyperspectral camera focal center $\mathbf{C}_h$ and the conventional camera focal center $\mathbf{C}_c$. The epipole $\mathbf{e}_h$ is the point at which the line from $\mathbf{C}_h$ to $\mathbf{C}_c$ intersects the line $\mathbf{l}_h$. The epipole $\mathbf{e}_c$ is the point where the line from $\mathbf{C}_c$ to $\mathbf{C}_h$ crosses the image plane of the conventional camera. This is illustrated in Figure 4. By making the epipole $\mathbf{e}_h$ lie on $\mathbf{l}_h$ such that $\mathbf{e}_h^T \mathbf{l}_h = 0$, $\mathbf{l}_h$ becomes an epipolar line. From epipolar geometry, it is known that each of the epipolar lines
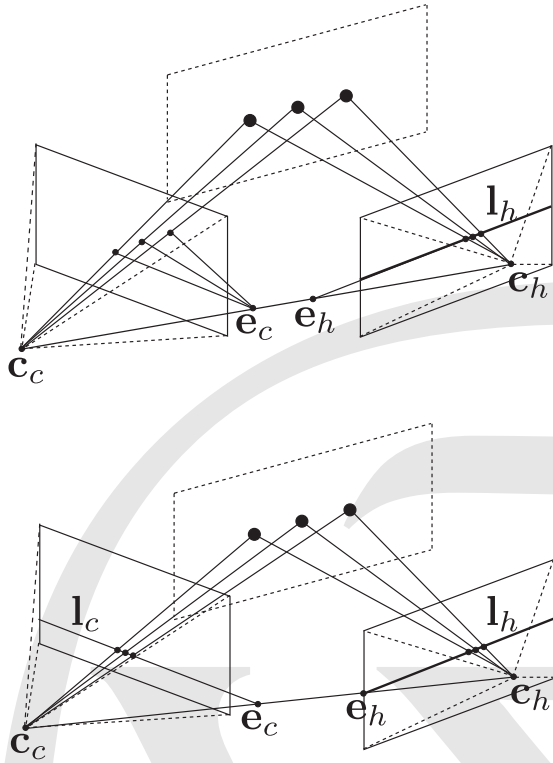
Figure 4. Effect of the world point depth over the projection of the hyperspectral camera line onto the conventional camera, with different alignments between cameras. Top: The world points lie on the same plane and are projected on a line on the conventional camera, but the position of this line depends on the point depths. The projections of these points would be part of a different line if their depths changed. Bottom: The hyperspectral line is an epipolar line, i.e., $\mathbf{e}_c$ and $\mathbf{l}_h$ are coplanar. The points project over the same line in the conventional camera regardless of their depth.

in one camera plane has a corresponding epipolar line in the other. To find the line $\mathbf{l}_c$ in the conventional image plane that corresponds to $\mathbf{l}_h$, consider a line $\mathbf{k}$ in the hyperspectral camera plane not crossing $\mathbf{e}_h$. The point where $\mathbf{l}_h$ and $\mathbf{k}$ intersect is $\mathbf{x} = \mathbf{k} \times \mathbf{l}_h$. Then $\mathbf{l}_c = E\mathbf{x}$, where E is the Essential matrix between both cameras (Huang & Faugeras, 1989).

Any nonzero $\mathbf{p} \in \mathbb{R}^3$ can represent either a line or a point in projective geometry, and the line expressed by $\mathbf{p}$ is such that $\mathbf{p}$ as a point does not belong to the line. This can be verified easily since $\mathbf{p}^T \mathbf{p} \neq 0$. We need a line $\mathbf{k}$ that will never go through $\mathbf{e}_h$. Thus, the line with coordinates given by the epipole $\mathbf{e}_h$ is a good choice for $\mathbf{k}$. Then the epipolar line in the conventional camera plane corresponding to $\mathbf{l}_h$ can be found as

$$\mathbf{l}_c = E[\mathbf{e}_h \times \mathbf{l}_h]. \qquad (9)$$

From the constraints placed on $\mathbf{e}_h$, the only translation between cameras that is allowed is $\mathbf{T} = [X\ 0\ Z\ 1]^T$ in the hyperspectral camera frame. Rotation is only restricted by the need to have the points within the field of view of the camera. It is only when the hyperspectral line becomes an epipolar line that the points projected onto the hyperspectral camera frame can be found on a corresponding epipolar line in the conventional camera regardless of the 3D world point depths.

With the conditions for a line-to-line mapping between cameras established, the next step is to formulate a way to align the cameras such that Eq. (9) holds. The calibration target from Section 2 can be used as an alignment aid. The alignment procedure we suggest is as follows:

- Affix the hyperspectral camera to the carrying rig.
- Position the calibration target such that every control point is visible to the hyperspectral camera.
- Translate and rotate the conventional camera until every control point of the calibration target lies on the same line in the image plane.

4. HYPERSPECTRAL LINE-TO-IMAGE MAPPING

We propose an optimization task that finds the mapping between cameras for any scene. With the camera array aligned as in Section 3, the world points projected onto the hyperspectral camera line can be found over a single line in the conventional camera image plane. From Eq. (9), we know the line-to-line mapping between the hyperspectral and conventional cameras. However, the data in the hyperspectral image are a *line segment* in $\mathbf{l}_h$, which corresponds to a line segment in $\mathbf{l}_c$. While it is known that the world points projected onto $\mathbf{l}_h$ are also projected onto $\mathbf{l}_c$, the precise mapping between line segments is not known if the depth and orientation of the plane π_1 with respect to $\mathcal{F}_h$ and $\mathcal{F}_c$ are unknown. Finding a map between line segments involves finding a scale factor s and displacement d that scale the length and shift the position of the pixels.

The conventional camera captures grayscale intensity images, so every pixel performs an integration of the light intensity over the pass band of the sensor. In the case of the hyperspectral camera, an intensity image can be approximated at each spatial pixel by summing the responses at every frequency band. This allows a comparison between intensity values from both cameras after they are normalized, even though they may differ by some unknown scalar factor and offset.

Consider a sequence of n simultaneously captured hyperspectral and conventional images. The kth hyperspectral image can be considered as a real $f \times c$ matrix $\mathbf{G}_k$, where each element $g_{i,j}^k$ corresponds to the ith frequency band and the jth spatial component. There are f frequency bands, c spatial components, and $k = 1, \ldots, n$ such matrices for an n

image sequence. Consider the $n \times c$ matrix $\mathbf{V}$, where each element $v_{k,j}$ is given by

$$v_{k,j} = \sum_{i=1}^{f} g_{i,j}^{k}. \tag{10}$$

That is, each row of $\mathbf{V}$ is the intensity response of the hyperspectral camera in image k. Similarly, consider an $n \times m$ matrix $\mathbf{W}$ where the kth row is the pixel values of the line $\mathbf{l}_c$ that correspond to the kth $\mathbf{l}_h$.

To match each conventional image line segment to the corresponding hyperspectral line segment, we minimize the cost function

$$J_m(\mathbf{d}, \mathbf{s}, \mathbf{V}, \mathbf{W}) = \sum_{k=1}^{n} \frac{\sum_{i=1}^{m} v_{k,i} \cdot w_{k,\lfloor (i-d_k)s_k \rfloor}}{||\mathbf{v}_k|| \sqrt{\sum_{i=1}^{m} \left[w_{k,\lfloor (i-d_k)s_k \rfloor} \right]^2}}. \tag{11}$$

The vector $\mathbf{v}_k$ is the kth row of $\mathbf{V}$. The n-element vectors $\mathbf{d}$ and $\mathbf{s}$ are the displacements and the scale factors that define each line correspondence, and their elements are denoted as d_k and s_k, respectively. The cost function is based on the cosine similarity between signals. The locally optimal scaling and displacement vectors satisfy

$$\{\mathbf{d}_{\text{opt}}, \mathbf{s}_{\text{opt}}\} = \arg\min_{\mathbf{d},\mathbf{s}} J_m(\mathbf{d}, \mathbf{s}, \mathbf{V}, \mathbf{W}). \tag{12}$$

This optimization task is nonlinear in nature, and we have obtained our best results by applying the Nelder-Mead algorithm (Nelder & Mead, 1965). For initialization, we estimate an initial displacement by using normalized correlation between the scaled hyperspectral lines and their conventional camera equivalents. The initial scaling factor is the ratio between the conventional camera focal length and that of the hyperspectral camera.

5. IMAGE REGISTRATION

We have detailed a procedure to obtain a mapping between the hyperspectral camera data and the images captured by the conventional camera. These correspondences alone are not sufficient to create a hyperspectral *image* of the captured scene. It is still necessary to recover the motion of the hyperspectral camera over time in order to organize the data, i.e., to properly order and align the line segments imaged by the hyperspectral camera. To achieve this, we leverage approaches to combine multiple overlapping images, forming a single depiction of the captured scene from the conventional camera. Forming an image mosaic with the conventional camera images also provides a mapping between the relative positions of the camera when each image was captured. This, along with the mapping from points in the hyperspectral image to the conventional image described in Section 4, can enable spectroscopy of a given region.

5.1. Correlation-based Matching

One approach to mosaicing that has been applied to form hyperspectral images is to use correlation to find a similarity transform (Moroni et al., 2012). This approach works well when the motion of the camera is primarily translation over the X and/or Y axes. Since it can be a costly operation, correlation is often replaced with frequency-domain multiplication via fast Fourier transform.

The correlation between two images can provide information about the location of maximum similarity to overlap two images, but not about the degree of rotation or the difference in scale between them. To determine these parameters, it is necessary to perform the correlation operation for multiple Z-axis rotations and/or scalings. This adds to the computational cost of the operation, but it can provide accurate results for aircraft-mounted cameras following straight flight paths.

When the straight-path assumption is not satisfied, it is still possible to find the similarity transform that most closely matches the subsequent frames. However, as we show further below, the resulting imagery may not preserve the geometry of the original scene.

5.2. Feature-based Matching

When the imaged scenes are far away from the camera, we can approximate every world point as lying on a common plane. This assumption is of special interest while performing aerial or satellite photography. The points mapping between different images of such scenes can be characterized with a homography, which can then be used to create image mosaics. Let there be a set of 3D points restricted to lie in a plane $\pi_1 \subset \mathbb{R}^3$, and let two cameras capture images of the points. There exists a homography matrix $H \in \mathbb{R}^{3 \times 3}$ that relates the projection $\mathbf{p}_1$ of each point in the second camera, $\mathbf{p}_2$. This relationship is given by

$$\mathbf{p}_2 \sim H\mathbf{p}_1. \tag{13}$$

The homography matrix between two conventional camera views can be recovered by the four-point algorithm from point correspondences (Faugeras & Lustman, 1988; Ma, Soatto, Košecká, & Sastry, 2004). Coupling the four-point algorithm with random sample consensus (RANSAC) delivers an accurate homography matrix solution in the presence of noise and mismatches (Torr & Zisserman, 1999). This is useful if the correspondences are obtained using region features such as scale-invariant feature transform (SIFT) or speeded-up robust features (SURF). In our approach, we make use of SURF (Bay, Ess, Tuytelaars, & Van Gool, 2008). Its performance is comparable to SIFT for the class of motions considered here, while being computationally less expensive (Bauer, Sunderhauf, & Protzel, 2007).

The number of SURF features per image to retrieve was not set in advance, but more that 1,000 were extracted in every frame. A higher number of matches between SURF

points in different images is not the only factor related to the quality of the registration. Matching SURF features between image pairs requires a metric to evaluate the correspondences. The sum of squared differences (SSD) for a neighborhood of pixels around the candidate points provide a good indication of the match quality. The SSD can be coupled with a distance threshold to discard unreasonable matches, under the standard assumptions of optical flow for features (constant intensity and smooth motion across frames).

The quality of the registration is also greatly affected by the residual error after computing H. The RANSAC algorithm provides a good estimate in the presence of outliers, even if some incorrect point matches are not properly discarded with the SSD and distance metric. The resulting H matrix will still need to be refined by the application of nonlinear optimization (e.g., the Levenberg-Marquardt algorithm) to minimize the reprojection error. At the end of the optimization, the homography matrix for a single image pair is obtained.

One approach to construct a mosaic from several images of a planar scene is to find the homographies for every image pair. Then the images are warped to register to a reference image chosen among them. The problem with this approach is that errors accumulate, resulting in distortion effects. To avoid this, we use the approach of Shum & Szeliski (2000). Consider a set of n images $\mathcal{I} = I_1, \ldots, I_n$ of a planar scene, with enough overlap and matching feature pairs to successfully recover the homographies. In image I_k, let there be m feature points. The homogeneous coordinates for the feature points in I_k can be combined to form a matrix $P \in \mathbb{R}^{3 \times m}$. Let $\mathcal{H}$ denote the set of n^2 homographies, with each element H_i^j being the homography between images I_i and I_j that satisfies $P_j = H_i^j P_i$. These relationships can be exploited in an optimization scheme to reduce registration errors in building the mosaic. Consider a cost function to minimize given by

$$J_h(\mathcal{H}, P_1, \ldots, P_n) = \sum_{i=1}^{n} \sum_{j=1}^{n} ||P_j - H_i^j P_i||^2 \qquad (14)$$

with the optimum being the solution to

$$\mathcal{H}_{\text{opt}} = \arg\min_{\mathcal{H}} J_h(\mathcal{H}, P_1, \ldots, P_n). \qquad (15)$$

We favor using the feature-based matching approach since it better preserves the underlying geometry of the imaged scene. To illustrate this point, consider Figure 5. It first shows a visible-light orthophoto from the Google Maps satellite image collection. We highlighted two features connected by a dashed line, and a rectangle emphasizes a creek. Note that the rectangle lies mostly to the right of the dashed line. The two images below compare the position of these features for the frequency-based and the feature-based approaches, respectively. The frequency-based mosaic on
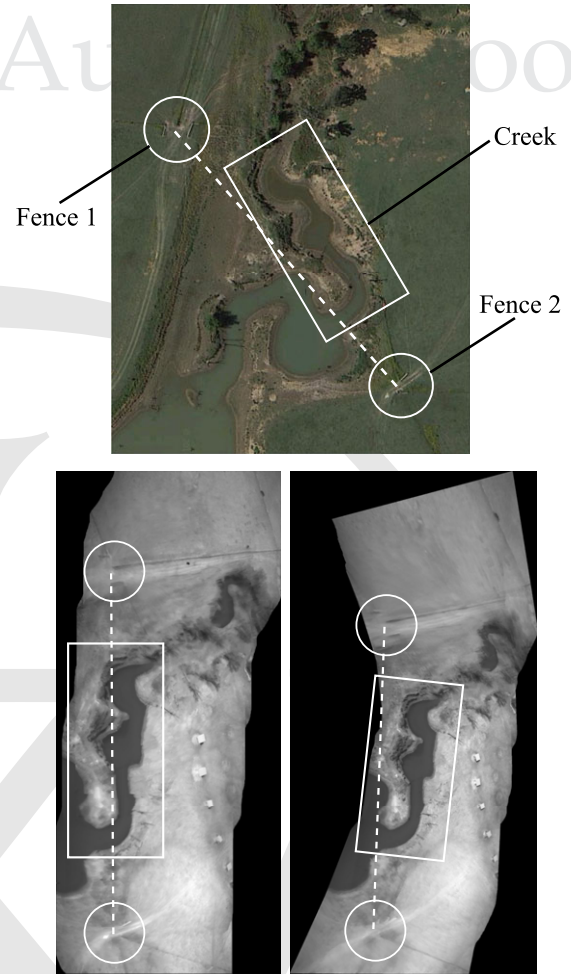

Figure 5. Comparison of the relative placement of some scene features between a reference orthophoto and the image mosaics from experimental data. The bottom left image is a mosaic built using frequency-based matching, while the bottom right image was assembled using feature-based matches. Only the latter preserves the geometry of the orthophoto.

the left does not preserve the geometry of the orthophoto, as the dashed line crosses over the creek. The feature-based mosaic, on the right, does preserve the relationship.

5.3. Hyperspectral Image Assembly

At this stage, there is enough information to construct the hyperspectral image. Using the line-to-line correspondences described in Section 3 and the scaling factors and the displacements between the hyperspectral and the conventional camera pixels described in Section 4, the positions of the hyperspectral camera points projected onto the conventional camera images can be recovered. Using these new point coordinates for the hyperspectral data and applying

the homographies from Eq. (15), a single hyperspectral image with all the frequency bands as layers is recovered.

The application of the homographies results in sparse data consisting of triplets of the form $\{x, y, F_{1,\dots,f}\}$, where x, y are image coordinates and $F_{1,\dots,f}$ is the set of all the intensity values for each of the frequency bands from the hyperspectral sensor. An interpolation procedure is needed to obtain a dense data set. The choice of interpolation algorithm is up to the specific application for the images. There are nonuniform interpolation techniques that can then be applied to the data, including linear interpolation, inverse distance weighting, nearest neighbors, kriging, etc. (Oliver & Webster, 1990; Ruprecht, Nagel, & Müller, 1995). The interpolated result is also known as a *data cube*.

Qualitatively, the proposed approach results in mosaics that better fit orthorectified image databases than correlation-based approaches. Validating the geometric accuracy generally requires reference orthorectified imagery to match the hyperspectral image (Laliberte, Winters, & Rango, 2008) or georeferenced ground control points indicated by reflective markers on a surveyed area (Rocchini & Di Rita, 2005). It also requires additional data, such as the external orientation of the aircraft and camera array, the camera position as determined from GPS points, and a digital elevation model. This work demonstrated hyperspectral image creation using only image data, but quantitative analysis will be performed prior to any application in remote sensing.

6. RESULTS

We present experiments conducted with a low-altitude UAV. We employed a Sony XCG-V60E monochrome conventional camera and a custom-made hyperspectral camera manufactured by Surface Optics, based on the AVT Prosilica GC 655. Both cameras have 640 pixels of horizontal resolution. The conventional camera has 480 pixels of vertical resolution, while the hyperspectral vertical information contains the frequency response in 120 different bands, with wavelengths covering a range of 400–1,000 nm. The rate of acquisition for the system is 90 frames per second for both cameras. Our camera array is mounted on an aluminum rail, shown in Figure 6. The radiometric calibration of the sensor was based on manufacturer spectral sensitivity data.

We used a piloted, radio-controlled airplane to perform the data collection. The plane, pictured in Figure 7, is capable of carrying a 2.5 kg payload with its electric motor. It is equipped with a micro-ATX PC and GigE interface to the cameras. The airplane was flown over a designated RC field. The imaged area included grassland and ponds for livestock. The airplane height above ground was set below 100 m, with an average of 60 m, and the wind was blowing at an average of 30 km/h from the south.

The hyperspectral camera has many applications in vegetation studies, such as precision agriculture, by as-

Figure 6. Experimental camera array. The hyperspectral camera has a cylindrical shape and it is shown in the middle, with the smaller conventional camera to its left.

Figure 7. Low-altitude airplane used to carry the camera array.

sessing plant health using narrowband indices. A study of the application of various narrowband indices for plant health and stress assessment can be found in Zarco-Tejada et al. (2005). One useful quantity that can be computed from hyperspectral data is the Normalized Difference Vegetation Index (NDVI) (Tucker, 1979). The NDVI combines the reflectance of objects to visible and near-infrared light wavelengths to estimate the vegetation content of a region. Healthy vegetation absorbs most of the visible light that reaches it, while reflecting most of the infrared radiation. Unhealthy or dormant vegetation reflects more visible light with respect to near-infrared. For each imaged point, the NDVI is computed as

$$\text{NDVI} = \frac{\text{NIR} - \text{VIS}}{\text{NIR} + \text{VIS}},$$

where NIR stands for near-infrared intensity and VIS is the visible light intensity. The range of values for the NDVI is $[-1, 1]$, where 1 represents healthy, dense vegetation. Values
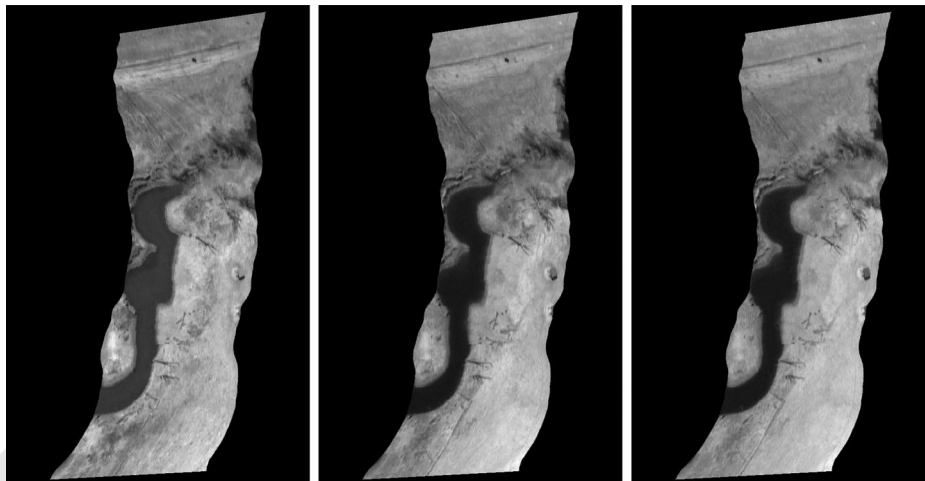
Figure 8. These images show some spectral bands that can be retrieved from the hyperspectral data. From left to right: R_{670}, related to the chlorophyll absorption in plants; R_{725}, in the edge of the red band; and R_{800}, within the near-infrared.

near 0 may represent concrete, dirt, or otherwise vegetation-depleted regions, and values near -1 typically correspond to deep water or clear sky. Let us refer to individual narrowband images as R_n, where n is the wavelength of the band. There are narrowband versions of the NDVI, such as

$$\text{NDVI}_n = \frac{R_{774} - R_{677}}{R_{774} + R_{677}}.$$

A sample of the constructed hyperspectral datacube can be seen in Figure 8. These are some narrowbands associated with remote sensing of vegetation: R_{670} is related to the chlorophyll absorption of the plants, R_{725} is the edge of the red portion of the spectrum and has been associated with chlorophyll content as well, and R_{800} is at the beginning of the near-infrared. The airplane flew a horizontal distance of 200 m while capturing this particular set of images.

For each image sequence, we show three results. The first image shows the mosaic assembled from the conventional camera data, with an overlay of the intensity image derived from the hyperspectral data. This intensity image is composed by the sum of every hyperspectral channel. The second image shows the mosaic from the conventional camera with the NDVI$_n$ data overlayed. We used a color map where blue tones correspond to areas with no vegetation and healthy plants begin to appear as red tones, with dark red being the most dense and healthy. Finally, the third image is a pseudocolor representation of the scene, on top of the conventional camera mosaic. To build the pseudocolor image, we took R_{700}, R_{550}, and R_{490} to represent the colors red, green, and blue, respectively.

We selected a few regions of interest from the available imagery in order to present a variety of objects, as well as to emphasize some aircraft motions that would make hyperspectral imaging impossible without the approach described here. The compiled scenes include grass, water,

trees with and without foliage, bale sheds, fences, dirt roads, etc. The flights were carried out over the month of February 2014 near Dallas, Texas, at a time of year when most vegetation was dormant. The first sequence, pictured in Figure 9, covers a region over a pond approximately 200 m long. The water had a green hue, as visible in the last image, but as expected it appeared to have low NDVI$_n$ values. Likewise, the roof from the shed covered by the hyperspectral imagery appears in a dark blue hue due to it being highly reflective in the visible frequency bands but absorptive in the NIR bands. This fact is also evident from depictions of the shed in Figure 8, which correspond to the same image sequence. The amount of detail preserved is notable, considering the sparseness of the original data and the absence of pose information of the plane with respect to the scenery.

Figure 10 illustrates a more difficult imaging scenario. Here the airplane was banking during a turning motion. The perspective effect is noticeable. A mixture of small ponds and some trees over mostly dormant grass comprises the scene. The buildings shown near the top give an indication of the banking angle of the airplane, and yet the image mosaic and the hyperspectral image match seamlessly. The straight-line flight distance for this sequence was 350 m. A last example is shown in Figure 11. This area included mostly grass in different health conditions, from dry to green. The airplane was pushed by a wind gust while completing a turn, giving rise to the shape shown for the hyperspectral data. Even under these motions, there are no severe mismatches or gaps in the resulting images. The flight distance for this image set was 150 m.

As can be seen from the results, our approach achieves a precise alignment between the hyperspectral data and the conventional camera mosaic. This remains true even in the presence of large disturbances due to external factors such as wind gusts or vibrations from the UAV motor.
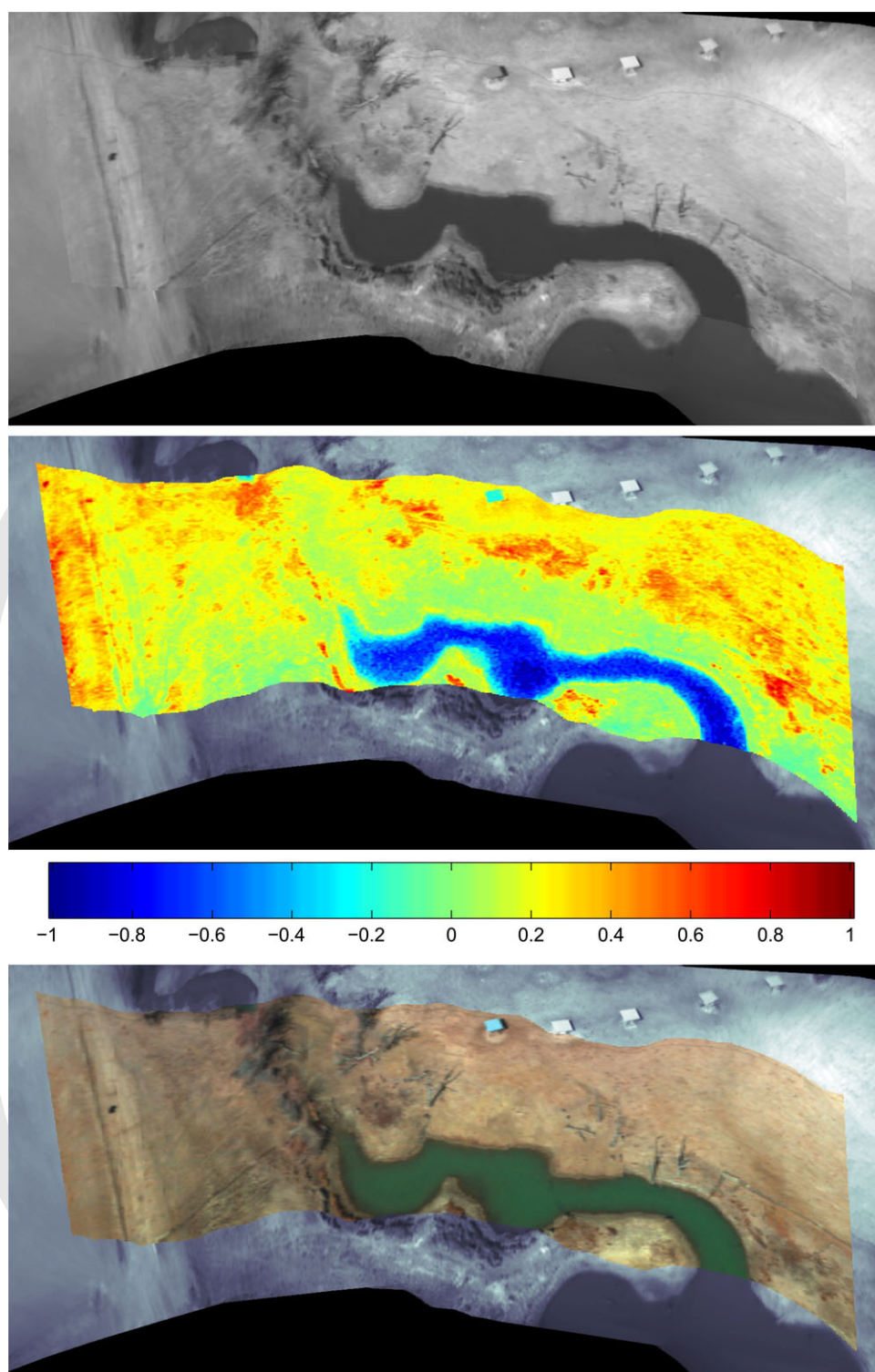
Figure 9. Hyperspectral imaging of a rural landscape. Top image: sum of every spectral channel from the HS image, overlaid on top of the visible camera mosaic. Middle image: Normalized Difference Vegetation Index. Bottom image: pseudocolor from red, green, and blue channels.
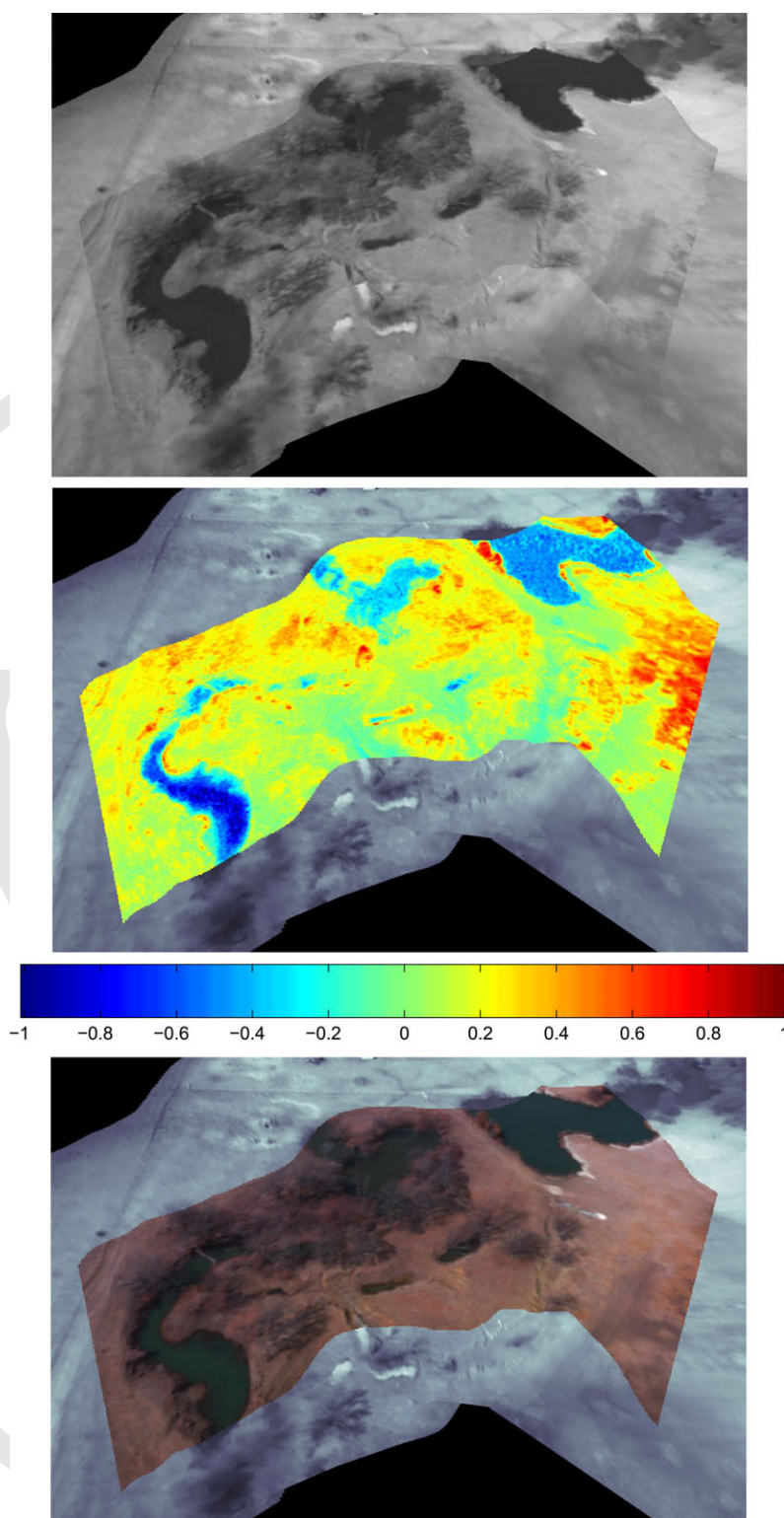
Figure 10. Severe perspective effect due to the aircraft banking while turning. The top image corresponds to intensity, followed by the NDVI$_n$ and pseudocolor images.
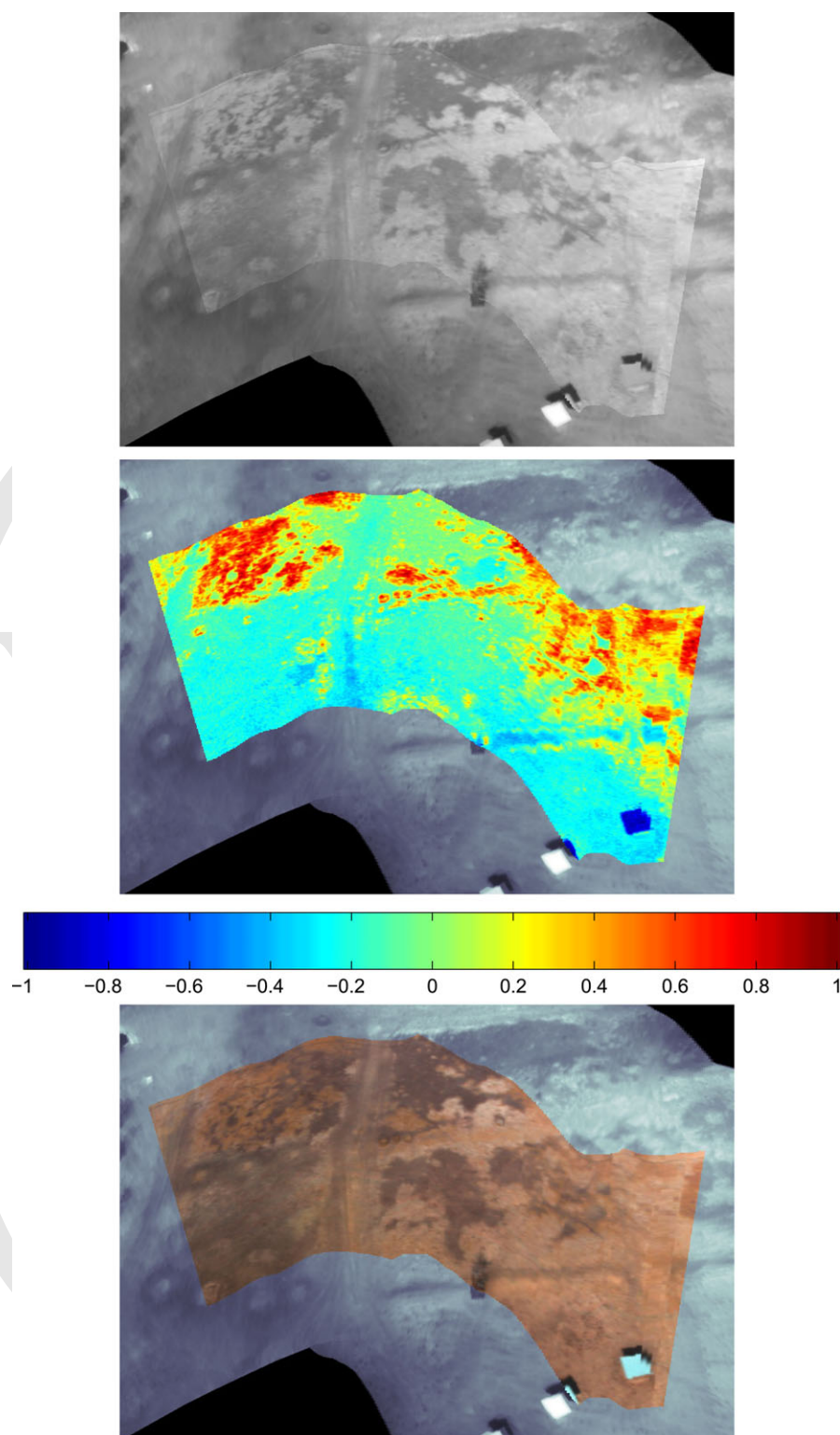
Figure 11. An scene that shows the effect of wind on the airplane while it was banking. Intensity, NDVI_n, and pseudocolor images are shown.

The hyperspectral images retain a level of detail on a par with the conventional camera images, with little blurring or distortion.

7. CONCLUSION

Based on an auxiliary conventional camera, we have presented a method to acquire images with a pushbroom hyperspectral sensor. Our approach maps each hyperspectral line to a line in the conventional camera image plane. We showed that this can only be achieved for arbitrary world point depths when the hyperspectral line is an epipolar line too. Two variables that need to be determined given this line-to-line mapping are the scale of each hyperspectral line segment and its displacement with respect to the conventional camera line segment over which it is mapped. Nonlinear optimization through direct search methods yields the best results when dealing with such a task. We have tested parallel implementations of these optimization algorithms that resulted in promising reductions in computation time, making hyperspectral image creation more practical.

The final assembly of a hyperspectral image involves finding the homographies between conventional camera image pairs. This is done to create an image mosaic and at the same time the hyperspectral image. The data cubes produced by the application of our technique show remarkable alignment with the conventional camera mosaics, delivering high-resolution spectroscopy from a low-cost UAV. We must stress the inexpensiveness of the equipment we used when compared to other solutions. Other than the hyperspectral camera, the rest of the platform, including the airplane, the secondary camera, and the onboard computer, has a lower cost than some software packages.

Several challenges can to be addressed by our method, including the absence of pose information for the cameras while they captured the images, and the presence of external disturbances such as wind gusts. We showed that assuming that the scene is planar works in practice, even if the terrain is not flat. Future research will focus on extending the techniques described to cover wider areas with multiple flight lines. Furthermore, we plan to apply this research to specific field studies in remote sensing. An important task to perform during these studies will be to combine our technique with the placement of ground control points so that the perspective transformation between the generated hyperspectral images and the ground surface enables the creation of a fully georeferenced data set.

ACKNOWLEDGMENTS

REFERENCES

Abdel-Aziz, Y. (1971). Direct linear transformation from comparator coordinates in close-range photogrammetry. In ASP Symposium on Close-Range Photogrammetry in Illinois.

Al-Moustafa, T., Armitage, R. P., & Danson, F. M. (2012). Mapping fuel moisture content in upland vegetation using airborne hyperspectral imagery. Remote Sensing of Environment, 127, 74–83.

Asmat, A., Milton, E., & Atkinson, P. (2011). Empirical correction of multiple flightline hyperspectral aerial image mosaics. Remote Sensing of Environment, 115(10), 2664–2673.

Bauer, J., Sunderhauf, N., & Protzel, P. (2007). Comparing several implementations of two recently published feature detectors. In Proceedings of the International Conference on Intelligent and Autonomous Systems (vol. 6).

Bay, H., Ess, A., Tuytelaars, T., & Van Gool, L. (2008). Speeded-up robust features (SURF). Computer Vision and Image Understanding, 110(3), 346–359.

Brown, D. C. (1966). Decentering distortion of lenses. Photometric Engineering, 32(3), 444–462.

Caballero, F., Merino, L., Ferruz, J., & Ollero, A. (2009). Unmanned aerial vehicle localization based on monocular vision and online mosaicking. Journal of Intelligent and Robotic Systems, 55(4-5), 323–343.

Draréni, J., Roy, S., & Sturm, P. (2011). Plane-based calibration for linear cameras. International Journal of Computer Vision, 91(2), 146–156.

Faugeras, O. D., & Lustman, F. (1988). Motion and structure from motion in a piecewise planar environment. International Journal of Pattern Recognition and Artificial Intelligence, 2(03), 485–508.

Goetz, A. (2009). Three decades of hyperspectral remote sensing of the Earth: A personal view. Remote Sensing of Environment, 113(1), S5–S16.

Gupta, R., & Hartley, R. I. (1997). Linear pushbroom cameras. IEEE Transactions on Pattern Analysis and Machine Intelligence, 19(9), 963–975.

Hartley, R., & Zisserman, A. (2003). Multiple view geometry in computer vision. Cambridge, UK: Cambridge University Press.

Herweg, J., Kerekes, J., & Eismann, M. (2012). Hyperspectral imaging phenomenology for the detection and tracking of pedestrians. In 2012 IEEE International Geoscience and Remote Sensing Symposium (IGARSS) (pp. 5482–5485).

Honkavaara, E., Saari, H., Kaivosoja, J., Pölönen, I., Hakala, T., Litkey, P., Mäkynen, J., & Pesonen, L. (2013). Processing and assessment of spectrometric, stereoscopic imagery collected using a lightweight uav spectral camera for precision agriculture. Remote Sensing, 5(10), 5006–5039.

Hruska, R., Mitchell, J., Anderson, M., & Glenn, N. F. (2012). Radiometric and geometric analysis of hyperspectral

imagery acquired from an unmanned aerial vehicle. Remote Sensing, 4(9), 2736–2752.

Huang, T. S., & Faugeras, O. D. (1989). Some properties of the E matrix in two-view motion estimation. IEEE Transactions on Pattern Analysis and Machine Intelligence, 11(12), 1310–1312.

Kruse, F., Boardman, J., & Huntington, J. (2003). Comparison of airborne hyperspectral data and EO-1 Hyperion for mineral mapping. IEEE Transactions on Geoscience and Remote Sensing, 41(6), 1388–1400.

Laliberte, A. S., Winters, C., & Rango, A. (2008). A procedure for orthorectification of sub-decimeter resolution imagery obtained with an unmanned aerial vehicle (UAV). In Proceedings of the ASPRS Annual Conference (pp. 08–047).

Lucieer, A., Malenovskỳ, Z., Veness, T., & Wallace, L. (2014). HyperUAS–Imaging spectroscopy from a multirotor unmanned aircraft system. Journal of Field Robotics.

Ma, Y., Soatto, S., Košecká, J., & Sastry, S. (2004). An invitation to 3D vision. New York: Springer-Verlag.

Monteiro, S. T., Minekawa, Y., Kosugi, Y., Akazawa, T., & Oda, K. (2007). Prediction of sweetness and amino acid content in soybean crops from hyperspectral imagery. ISPRS Journal of Photogrammetry and Remote Sensing, 62(1), 2–12.

Moroni, M., Dacquino, C., & Cenedese, A. (2012). Mosaicing of hyperspectral images: The application of a spectrograph imaging device. Sensors, 12(8), 10228–10247.

Nelder, J. A., & Mead, R. (1965). A simplex method for function minimization. The Computer Journal, 7(4), 308–313.

Oliver, M. A., & Webster, R. (1990). Kriging: A method of interpolation for geographical information systems. International Journal of Geographical Information System, 4(3), 313–332.

Ramirez-Paredes, J.-P., Lary, D., & Gans, N. (2013). Terrestrial hyperspectral imaging by integrating visible light mosaics and a line-scan camera. In AIAA Infotech@Aerospace (I@A) Conference, Boston: American Institute of Aeronautics and Astronautics.

Rocchini, D., & Di Rita, A. (2005). Relief effects on aerial photos geometric correction. Applied Geography, 25(2), 159–168.

Ruprecht, D., Nagel, R., & Müller, H. (1995). Spatial free-form deformation with scattered data interpolation methods. Computers & Graphics, 19(1), 63–71.

Salvi, J., Armangué, X., & Batlle, J. (2002). A comparative review of camera calibrating methods with accuracy evaluation. Pattern Recognition, 35(7), 1617–1635.

Schechner, Y., & Nayar, S. (2002). Generalized mosaicing: Wide field of view multispectral imaging. IEEE Transactions on Pattern Analysis and Machine Intelligence, 24(10), 1334–1348.

Shum, H.-Y., & Szeliski, R. (2000). Systems and experiment paper: Construction of panoramic image mosaics with global and local alignment. International Journal of Computer Vision, 36(2), 101–130.

Sidike, P., Khan, J., Alam, M., & Bhuiyan, S. (2012). Spectral unmixing of hyperspectral data for oil spill detection. In SPIE Optical Engineering+ Applications (pp. 84981B–84981B). International Society for Optics and Photonics.

Smith, K., Steven, M., & Colls, J. (2004). Use of hyperspectral derivative ratios in the red-edge region to identify plant stress responses to gas leaks. Remote Sensing of Environment, 92(2), 207–217.

Stratoulias, D., Balzter, H., Zlinszky, A., & Tóth, V. R. (2015). Assessment of ecophysiology of lake shore reed vegetation based on chlorophyll fluorescence, field spectroscopy and hyperspectral airborne imagery. Remote Sensing of Environment, 157, 72–84.

Szeliski, R. (1996). Video mosaics for virtual environments. IEEE Computer Graphics and Applications, 16(2), 22–30.

Torr, P. H., & Zisserman, A. (1999). Vision algorithms: Theory and practice, Number 1883 in Lecture Notes in Computer Science (pp. 278–294). Springer-Verlag.

Tucker, C. J. (1979). Red and photographic infrared linear combinations for monitoring vegetation. Remote Sensing of Environment, 8(2), 127–150.

Turner, D., Lucieer, A., & Watson, C. (2012). An automated technique for generating georectified mosaics from ultra-high resolution unmanned aerial vehicle (UAV) imagery, based on structure from motion (SfM) point clouds. Remote Sensing, 4(5), 1392–1410.

Vagni, F. (2007). Survey of hyperspectral and multispectral imaging technologies. Technical Report TR-SET-065-P3, NATO Science and Technology Organization.

Zarco-Tejada, P. J., Berjón, A., López-Lozano, R., Miller, J., Martín, P., Cachorro, V., González, M., & De Frutos, A. (2005). Assessing vineyard condition with hyperspectral indices: Leaf and canopy reflectance simulation in a row-structured discontinuous canopy. Remote Sensing of Environment, 99(3), 271–287.

Zarco-Tejada, P. J., González-Dugo, V., & Berni, J. A. (2012). Fluorescence, temperature and narrow-band indices acquired from a UAV platform for water stress detection using a micro-hyperspectral imager and a thermal camera. Remote Sensing of Environment, 117, 322–337.

Zhang, Z. (2000). A flexible new technique for camera calibration. IEEE Transactions on Pattern Analysis and Machine Intelligence, 22(11), 1330–1334.

QUERIES

Q1: Figures 2, 3, 5, 6, 7, 9, 10, 11 are in color in the source files. Figures appear in color online at no cost to you. If you would like any figure to appear in color in the print issue, please advise and we will send you a formal quote for the cost. Otherwise they will appear in black and white in the print issue and in color online.

Q2: If desired, one proof page may appear in color in the print issue at no charge. Please indicate the page you would like printed in color, if any. Any additional figures can be in color for a charge of $850 per page.

Q3: Author: Please confirm that given names (red) and surnames/family names (green) have been identified correctly.

Q4: Author: Please check.

Q5: Author: Please provide the volume and page numbers if available.